Acta Geochim (2019) 38(3):376–390
https://doi.org/10.1007/s11631-019-00332-2

ORIGINAL ARTICLE

Using trace elements of magnetite to constrain the origin of the Pingchuan hydrothermal low-Ti magnetite deposit in the Panxi area, SW China

Yanjun Wang[1,2] · Weiguang Zhu[1] · Hong Zhong[1,2] · Zhongjie Bai[1] · Junhua Yao[1,2] · Chong Xu[1,2]

Received: 8 January 2019 / Revised: 19 February 2019 / Accepted: 12 March 2019 / Published online: 22 March 2019

Abstract The Pingchuan iron deposit, located in the Yanyuan region of Sichuan Province, SW China, has an ore reserve of 40 Mt with ~ 60 wt% Fe. Its genesis is still poorly understood. The Pingchuan iron deposit has a paragenetic sequence of an early Fe-oxide–Pyrite stage (I) and a late Fe-oxide–pyrrhotite stage (II). Stage I magnetite grains are generally fragmented, euhedral–subhedral, large-sized crystals accompanying with slightly postdated pyrite. Stage II magnetite grains are mostly unfragmented, anhedral, relatively small-sized grains that co-exist with pyrrhotite. Combined with micro-textural features and previously-obtained geochronological data, we consider that these two stages of iron mineralization in the Pingchuan deposit correspond to the Permian ELIP magmatism and Cenozoic fault activity event. Both the Stage I and II magnetites are characterized with overall lower contents of trace elements (including Cr, Ti, V, and Ni) than the ELIP magmatic magnetite, which suggests a hydrothermal origin for them. "Skarn-like" enrichment in Sn, Mn, and Zn in the Stage I magnetite grains indicate significant material contributions from carbonate wall-rocks due to water–rock interaction in ore-forming processes. Stage II magnetite grains contain higher Mn concentrations than Stage I magnetite grains, which possibly implies more contribution from carbonate rocks. In multiple-element diagrams, the Stage I magnetite shows systematic similarities to Kiruna-type magnetite rather than those from other types of deposits. Combined with geological features and previous studies on oxygen isotopes, we conclude that hydrothermal fluids have played a key role in the generation of the Pingchuan low-Ti iron deposit.

Keywords SW China · Pingchuan iron deposit · Low-Ti iron deposit · Hydrothermal magnetite

1 Introduction

The ~ 260 Ma Emeishan Large Igneous Province formed a massive volcanic succession of predominately basaltic flows and pyroclastics, and minor picrite and trachyte/rhyolite, with associated numerous ultramafic–mafic to felsic plutons in southwestern China (Chung and Jahn 1995; Zhang et al. 2006; Shellnutt et al. 2012). Along with the mantle plume event, several world-class magmatic Fe–Ti–V deposits, including the Taihe, Baima, Hongge, and Panzhihua deposits, occurred in the western Yangtze Block (Song et al. 2005, 2009, 2013; Zhou et al. 2005; Bai et al. 2012a, b; Chen et al. 2014). These deposits have attracted a lot of interest of many researchers due to their large quantity of Fe–Ti–V oxide ores with a grade at ~ 33 wt% Fe (Ma et al. 2003). Other than magmatic, high-Ti iron deposits, there are also low-Ti iron deposits, represented by the Pingchuan, Niuchang and Lanzhichang deposits, within the ELIP. The low-Ti iron deposits are characterized with relatively higher iron ore grade (> 40 wt% Fe) and smaller reserves (< 50 Mt iron ores). Their origin is still poorly understood because little attention has been paid to them. In this study, we present a microphotographic study and in-situ LA–ICP–MS trace elements of magnetite grains for the Pingchuan deposit. This dataset would allow us to explore

✉ Weiguang Zhu
zhuweiguang@vip.gyig.ac.cn

[1] State Key Laboratory of Ore Deposit Geochemistry, Institute of Geochemistry, Chinese Academy of Sciences, Guiyang 550081, China

[2] University of Chinese Academy of Sciences, Beijing 100049, China

the origin of magnetite from the Pingchuan deposit and further compare them with magnetite from other types of deposits, thus shedding light on the genesis of the low-Ti iron deposit.

2 Geological background and sampling

The Yangtze Block is separated from the North China Block to the north, the Cathaysia Block to the south, the Songpan–Ganzi fold belt to the northwest and the Simao Block to the southwest. The study area is located in the western Yangtze Block. The western part of the block consists of a Paleo–Mesoproterozoic basement, represented by the Dahongshan, Hekou, Kunyang, and Huili Groups. These groups are mainly comprised of low-grade metasedimentary rock with felsic and mafic metavolcanic interlayers. Numerous mid-Neoproterozoic igneous rocks, dominated by felsic intrusive and extrusive rocks with subordinate ultramafic–mafic lavas and dikes, also crop out in the region (Li et al. 2003, 2006; Zhou et al. 2006). The basement is overlain by Sinian (850–610 Ma) to Permian strata of clastic, carbonate and meta-volcanic rocks with a total sequence more than 9 km (SBGMR 1991).

The Pingchuan region in Sichuan Province has a well-preserved sedimentary sequence from Early Carboniferous to Early Permian. The Carboniferous strata include the early argillaceous limestones of Weining Formation and the late sandstones and limestones of Mapping Formation. The Early Permian rocks are characterized by the Shuhe, Yangxin (Maokou) and Pingchuan Formations, mainly consisting of limestones with minor siltstone and shale, from bottom up. Late Permian Emeishan volcanic succession overlies these rocks. As shown in Figs. 1 and 2, abundant ELIP-associated $\sim$ 260 Ma mafic and ultramafic intrusions also intrude into these strata. The 260.0–260.3 Ma Dabanshan gabbro (Wang et al. 2012; Zeng et al. 2013; Liu et al. 2015b) crop out in the northeast of the Pingchuan iron deposit (Fig. 2a). Plenty of picritic dykes show intimate spatial association with the Pingchuan deposit (Figs. 2b, 3a). These picritic porphyry dykes were thought to be emplaced at $\sim$ 248 Ma (Zeng et al. 2013) on the bias of limited analytic data. Liu et al. (2015b) reported apatite U–Pb age of 245 $\pm$ 26 Ma for the Pingchuan iron deposit.

The Pingchuan iron deposit has an estimated reserve of 40 Mt iron ores at $\sim$ 60 wt% Fe. Orebodies are generally in stratiform, lentoid, irregular and vein shapes. Iron ores, despite massive, brecciated, disseminated and stockwork types, mainly contain magnetite with minor siderite and pyrite and variable gangue minerals like dolomite, calcite, apatite, and chlorite. Samples in this study are generally massive ores with high grade and were collected from the most important orebody I, which mainly develops in the contact zone between the picritic dykes and Yangxin (Maokou) limestones. Other orebodies such as orebody II, III and IV were either small in scale or has been mined out. Brecciated limestone and carbonate minerals-rich veins could be observed (Fig. 3b–d).

Fig. 1 **a** Schematic map showing the tectonic framework of China. ▶ **b** Schematic geologic map showing the distribution of the magmatic Fe–Ti–V oxide ores of the Emeishan Large Igneous Province in SW China (modified after Song et al. 2009). Red square is shown Fig. 2a

Under a microscope, magnetite grains are divided into two stages (Fig. 4). Stage I magnetite grains are euhedral–subhedral crystals with large size mostly $>$ 200 μm in diameter (Fig. 4a, b). Some grains even exhibit oscillatory zones, where tiny inclusions linearly occur along with lattice plane (Fig. 4b). Stage I magnetite grains are generally fragmented and surrounded by postdated sulfides (Fig. 4a–d), which are mostly anhedral pyrite grains. Locally, martitization occur along the fractures in massive magnetite (Fig. 4c). Whereas Stage II magnetite grains are characterized with relatively small-sized anhedral grains (mostly $<$ 200 μm). They usually contain abundant tiny gangue mineral inclusions, which distribute randomly within magnetite grains (Fig. 4e–f). Interestingly, Stage II magnetites have experienced little fragmentation and martitization. Sulfides (mostly pyrrhotite grains) occur along with or within these magnetite grains (Fig. 4e–f).

Microscopic observations suggest that the large-sized Stage I magnetite grains formed prior to pyrite and hematite, whereas the anhedral Stage II magnetite grains are almost synchronous with pyrrhotite. Stage I magnetite grains were significantly overprinted by fragmentation events, which have not affected Stage II magnetite grains, suggesting that Stage I magnetite formed earlier than Stage II magnetite. Therefore, the Pingchuan deposit has a paragenetic sequence of an early Fe-oxide (Stage I magnetite) and subsequent sulfide stage (pyrite), and a following late Fe-oxide (Stage II magnetite) and almost simultaneous sulfide stage (pyrrhotite).

3 Analytical method

Major element compositions of ore samples for the Pingchuan deposit were determined using X-ray fluorescence spectrometers (XRF) at ALS Chemex Co Ltd, Guangzhou. The analytical precision is generally better than 5%.

Magnetite grains in seven thin slices were chosen for LA–ICP–MS trace element determination. Analyses were conducted using a Coherent GeoLasPro 193-nm Laser

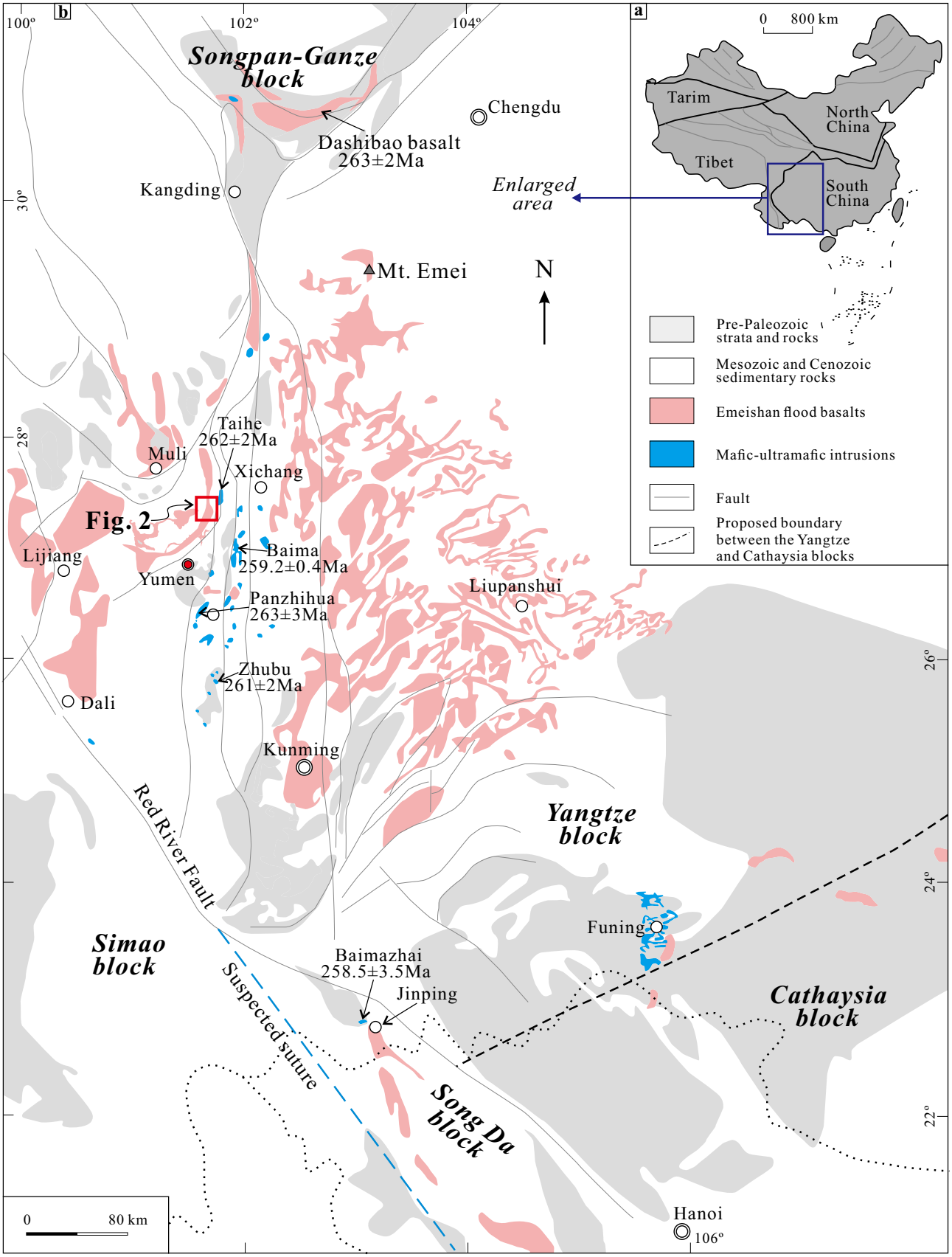
b
100°
102°
104°
30°
28°
26°
24°
22°
Songpan-Ganze block
Chengdu
Dashibao basalt
263±2Ma
Kangding
Enlarged area
Mt. Emei
N
Taihe
262±2Ma
Muli
Xichang
Fig. 2
Baima
259.2±0.4Ma
Lijiang
Yumen
Panzhihua
263±3Ma
Liupanshui
Zhubu
261±2Ma
Dali
Kunming
Red River Fault
Yangtze block
Simao block
Funing
Baimazhai
258.5±3.5Ma
Jinping
Suspected suture
Song Da block
Cathaysia block
Hanoi
106°
0 80 km
a
0 800 km
Tarim
North China
Tibet
South China
Pre-Paleozoic strata and rocks
Mesozoic and Cenozoic sedimentary rocks
Emeishan flood basalts
Mafic-ultramafic intrusions
Fault
Proposed boundary between the Yangtze and Cathaysia blocks

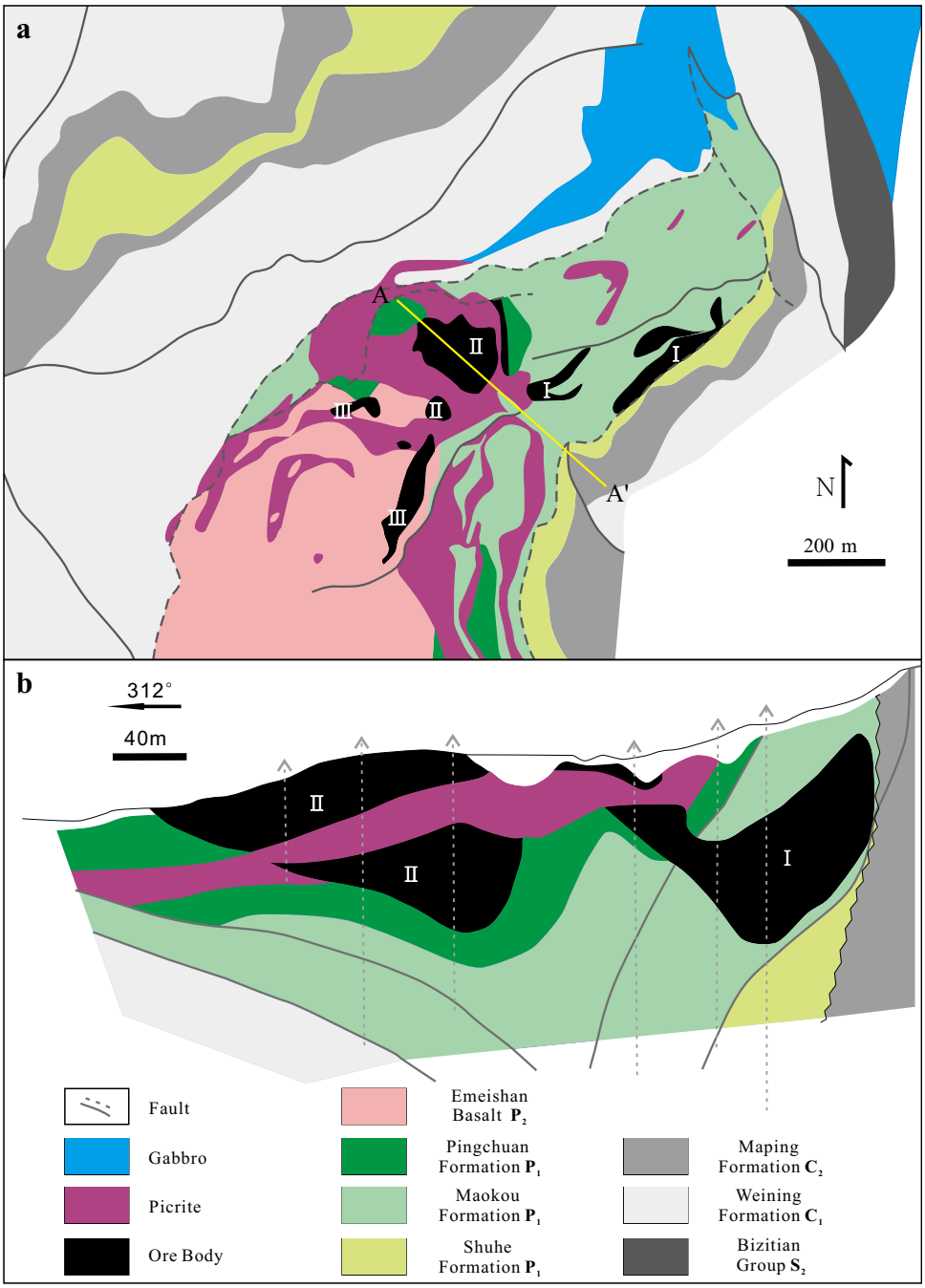

Fig. 2 **a** Geologic map of the Pingchuan iron deposit and **b** cross section of A–A′ exploration line (modified after Panxi Geological Team 1982)

Ablation system coupled with an Agilent 7700× ICP-MS at the SKLODG, IGCAS. Operating conditions and procedures are similar to those described in Gao et al. (2013). During the ablation, a repetition rate of 5 Hz and a laser spot size of 44 μm were adopted. Helium worked as the carrier gas and subsequently was mixed with argon gas in a T-connector prior to mass spectrometric analysis. Each analysis comprises 20s background on a gas blank and 60s analysis on unknown or standard materials. Several reference materials including BC-28, BCR-2G, GOR-128, GSE-1G and NIST 610 were analyzed to calibrate trace element contents with ^{57}Fe as the internal standard. Every eight unknown analyses were separated by GSE-1G with another standard to monitor time-dependent drift of sensitivity and mass discrimination. Offline data reduction was performed using ICPMSDataCal program (Liu et al. 2008) with $Fe^{2+}/\Sigma Fe$ values of 0.33 (Liu et al. 2015b).

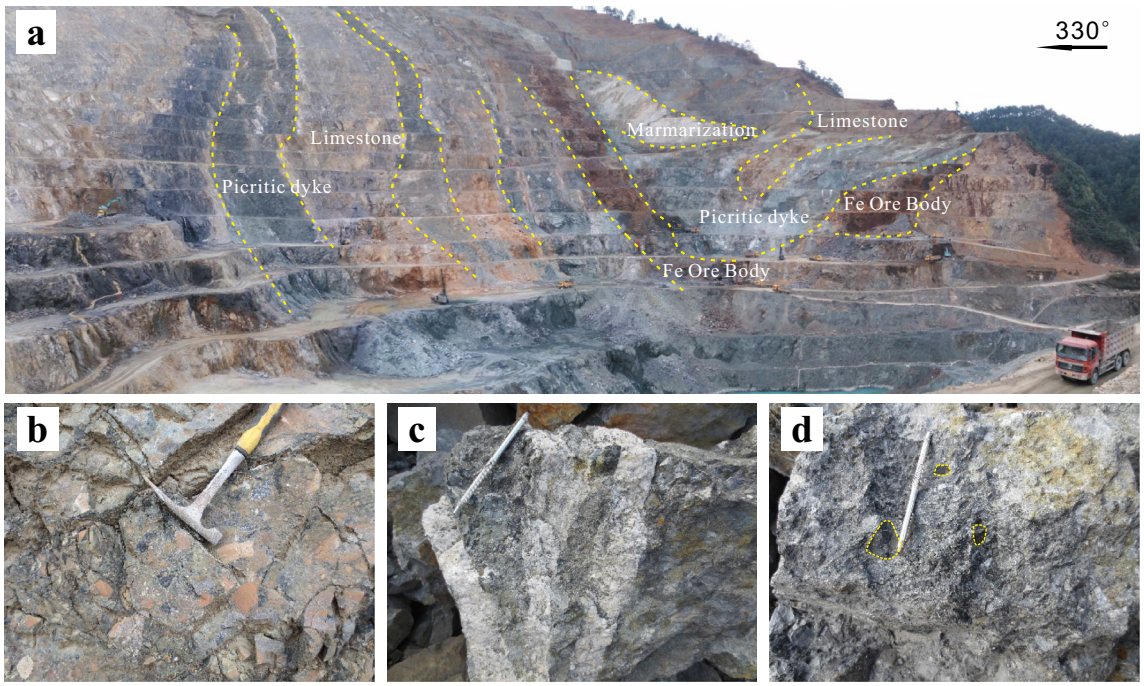

Fig. 3 **a** An overview of the Pingchuan open pit, showing field relationships of Fe orebodies, limestones and picritic dykes. **b–d** Representative brecciate rocks and carbonate veins in the mining district

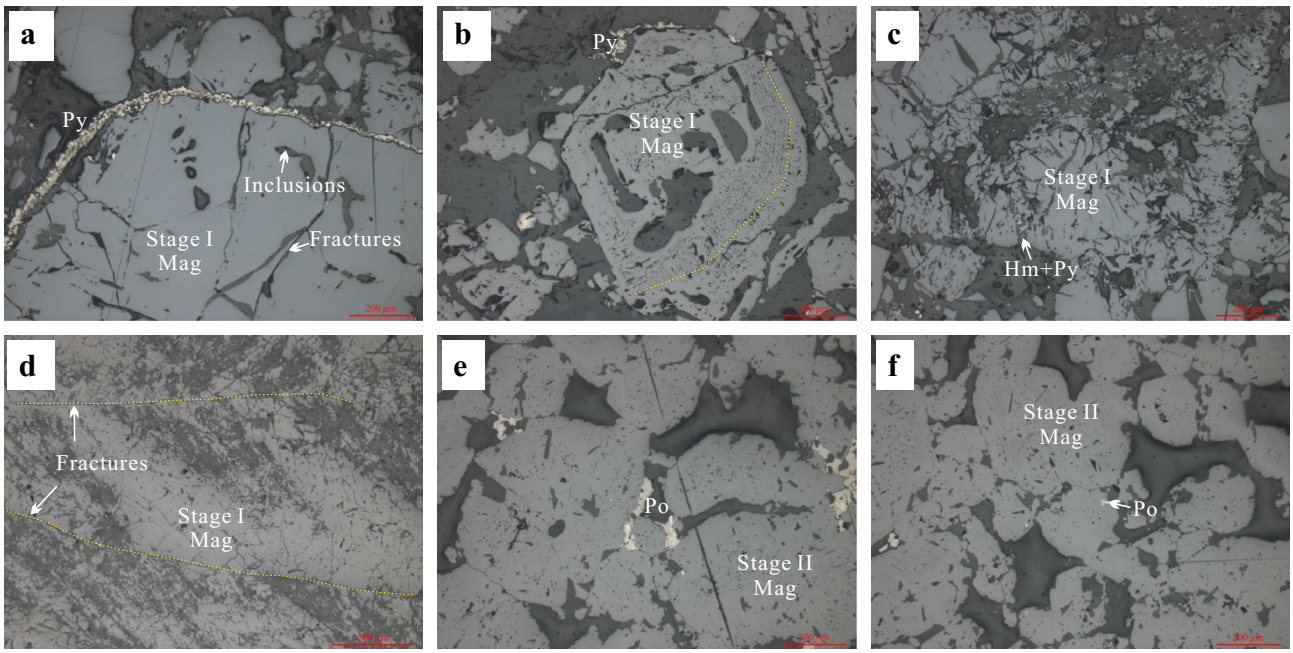

Fig. 4 Microphotographic pictures of **a** large-sized, **b** oscillatory zones, **c–d** fragmented Stage I magnetite and **e–f** unfragmented, Po-bearing Stage II magnetite. *Abbreviations*: *Hm* hematite, *Mag* magnetite, *Po* pyrrhotite, *Py* Pyrite

4 Results

Major elements of ore samples from the Pingchuan deposit are listed in Table 1. Ore samples are generally characterized with high contents of Fe_2O_3 (55.6–87.1 wt%; Fe = 38.9–61.0 wt%) and moderate MgO (2.68–7.82 wt%) and CaO (4.74–15.3 wt%) contents. Other oxides, such as TiO_2 and P_2O_5, are very low in the Pingchuan deposit. LOI values are high in these samples, agreeable with the presence of gangue carbonate minerals.

Trace elements of magnetite grains determined by LA–ICP–MS are presented in "Appendix". Stage I magnetite

Table 1 Major element (in wt%) compositions of ore samples from the Pingchuan deposit

Sample no.	KSL0720	KSL0721	KSL0723	KSL0726	KSL0728	KSL 0730	KSL0732	DB0901	DB0902	DB0903	DB0905	DB0906	DB 0909	DB0912	DB0913
SiO_2	5.63	0.28	0.31	0.62	0.21	0.43	0.29	0.35	0.35	0.15	0.37	0.16	0.93	2.74	0.93
TiO_2	0.12	0.01	0.01	0.01	0.01	< 0.01	0.01	0.01	0.01	< 0.01	0.01	0.01	< 0.01	0.01	0.01
Al_2O_3	2.22	0.03	0.05	0.08	0.05	0.05	0.04	0.03	0.06	0.03	0.09	0.06	0.04	0.04	0.08
Fe_2O_3	55.7	83.2	82.9	73.7	62.5	83.2	87.1	66.7	87.0	55.6	73.0	77.8	65.2	59.5	82.7
MnO	0.28	0.10	0.10	0.12	0.29	0.10	0.09	0.21	0.07	0.25	0.13	0.12	0.27	0.42	0.10
MgO	5.49	3.57	3.51	4.91	5.16	3.46	2.68	5.86	2.69	7.82	4.93	4.02	5.37	4.98	3.56
CaO	12.0	6.08	6.13	8.55	12.9	5.85	5.09	11.1	4.74	15.3	9.15	8.34	10.5	9.79	6.12
Na_2O	0.04	0.04	0.05	0.05	0.03	0.01	0.04	0.04	0.05	0.04	0.05	0.04	0.02	0.03	0.07
K_2O	0.02	0.01	0.01	0.01	0.01	< 0.01	0.01	0.01	0.01	0.01	0.01	0.01	< 0.01	0.01	0.02
P_2O_5	0.64	0.34	0.81	0.07	0.41	0.73	0.78	0.92	0.38	1.58	0.47	1.47	0.86	0.57	0.09
LOI.	13.7	5.41	3.62	7.66	14.1	4.50	2.89	9.97	1.70	16.4	7.88	7.10	12.4	19.9	5.88
Total	95.79	99.09	97.46	95.76	95.62	98.28	99.06	95.14	97.06	97.17	96.13	99.08	95.61	97.93	99.54
Fe	39.0	58.3	58.0	51.6	43.7	58.2	61.0	46.7	60.9	38.9	51.1	54.4	45.6	41.6	57.9

LOI loss on ignition

grains have substantial Si (678–7561 ppm), Mg (4.66–7158 ppm), Mn (9.19–322 ppm), Ca (4.55–3136 ppm), V (118–522 ppm), Zn (13.8–134 ppm), Al (12.0–129 ppm), Sn (10.7–38.2 ppm) and Co (0.30–38.5 ppm), which are much above detection limits. Ti (< 67.5 ppm), Cr (< 5.83 ppm), Ni (< 2.85 ppm), Ga (< 1.05 ppm), Sc (< 0.31 ppm) and other elements in these grains are either close to, or below detection limits. Stage II magnetite grains contain variable ranges of Si (624–3378 ppm), Mg (68.9–6998 ppm), Ca (2.50–1874 ppm), V (94.6–363 ppm), Zn (17.2–440 ppm), Al (19.3–257 ppm), Sn (8.32–69.7 ppm), Co (1.83–47.7 ppm), Ti (< 19.9 ppm), Cr (< 1.66 ppm), Ni (< 6.21 ppm), and Sc (< 0.12 ppm) similar to those of Stage I magnetite grains. However, most Stage II magnetite grains have slightly higher Mn (16.3–871 ppm) and lower Ga (< 0.59 ppm) than those of Stage I magnetite grains.

5 Discussion

5.1 Origin of magnetite

In the Pingchuan deposit, apatite grains accompanied with Stage I magnetite yields a U–Pb age of 245 ± 26 Ma and a fission-track age of 51.8 ± 4.9 Ma (Liu et al. 2015b), representing mineralization age and late thermal event, respectively. The former is overlapped with the ~ 260 Ma ELIP basalts and gabbros (e.g., Ali et al. 2005; Zhong et al. 2011; Wang et al. 2012; Zeng et al. 2013; Liu et al. 2015b) within error. Whereas, the latter event has experienced slow cooling at 70–24 Ma and fast cooling after 24 Ma (Liu et al. 2015b), coeval with ~ 67 Ma metamorphism record in picritic dikes (Zeng et al. 2013). This event is possibly linked to the thrust of the Cenozoic Jinqing fault (Ge 1984; Zhong et al. 2004) as suggested by Liu et al. (2015b). Combined with the contrasting fragmentation and inclusion-distribution features, we consider that the early Fe oxide (–sulfide) Stage is closely associated with the ELIP magmatic event and the late Fe oxide (–sulfide) Stage is intimately connected with Cenozoic fault activity. This interpretation is further supported by a decrease of sulfidation state from pyrite to pyrrhotite (Einaudi et al. 2003), which is identical to a drop of temperature and/or sulfur fugacity in the ore-forming system from magmatic-related to fault-related environments.

In Figs. 5 and 6, the Stage I and Stage II magnetite grains of the Pingchuan magnetite share very similar chemical compositions except for higher Mn contents in Stage II magnetites. Because high Mn is a significant feature for carbonate rocks, fault activities in carbonate rocks would lead to fluids enriched in Mn. Combined with geochronological data and micro-textural features, we suggest that the Stage II magnetites are recrystallized from

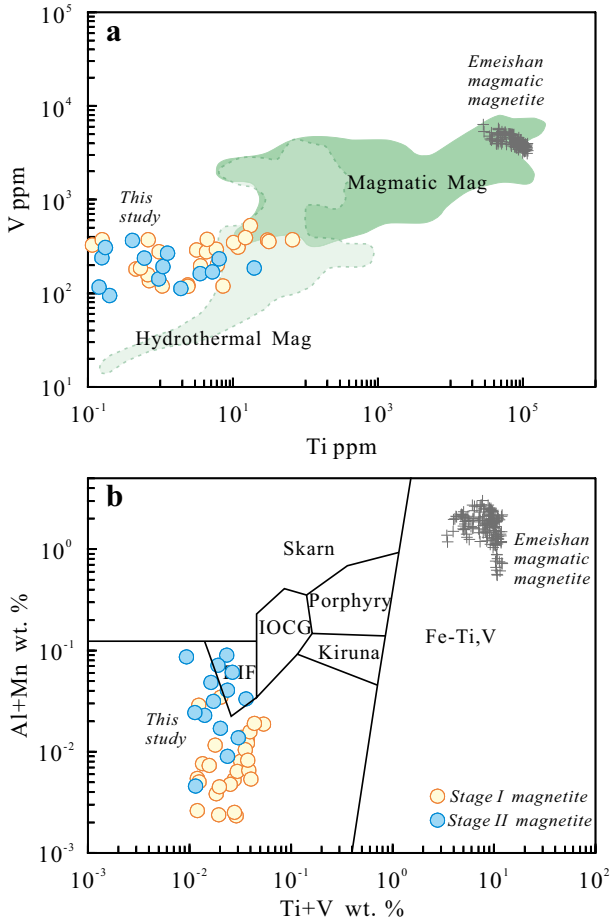

Fig. 5 **a** Chemical discrimination diagram for magnetite from magmatic and hydrothermal environments after Nadoll et al. (2014). **b** Chemical discrimination diagram for magnetite from different type deposits after Dupuis and Beaudoin (2011) modified by Nadoll et al. (2014). Data of Emeishan magmatic magnetite come from Liu et al. (2015a)

Stage I magnetite grains under the influence of fault-induced Mn-rich fluids. While the chemistry of the Stage I magnetites are genetically related to the Emeishan magmatism and would provide convincingly constraints on the origin of the Pingchuan deposit.

5.2 Genesis of the Pingchuan iron deposit

Elements such as Cr, Ti, V, and Ni usually show high contents in a magmatic system but low contents in a hydrothermal system, so they could be applied to discriminate magnetite formed in these systems (Dare et al. 2014; Knipping et al. 2015a; Nadoll et al. 2015; Wang et al. 2018). As shown in Figs. 5 and 6, both the Stage I and Stage II magnetite grains of the Pingchuan magnetite are with low concentrations of Ti, V, Ni, Cr, and Al + Mn, which are much lower than those in the regional coeval

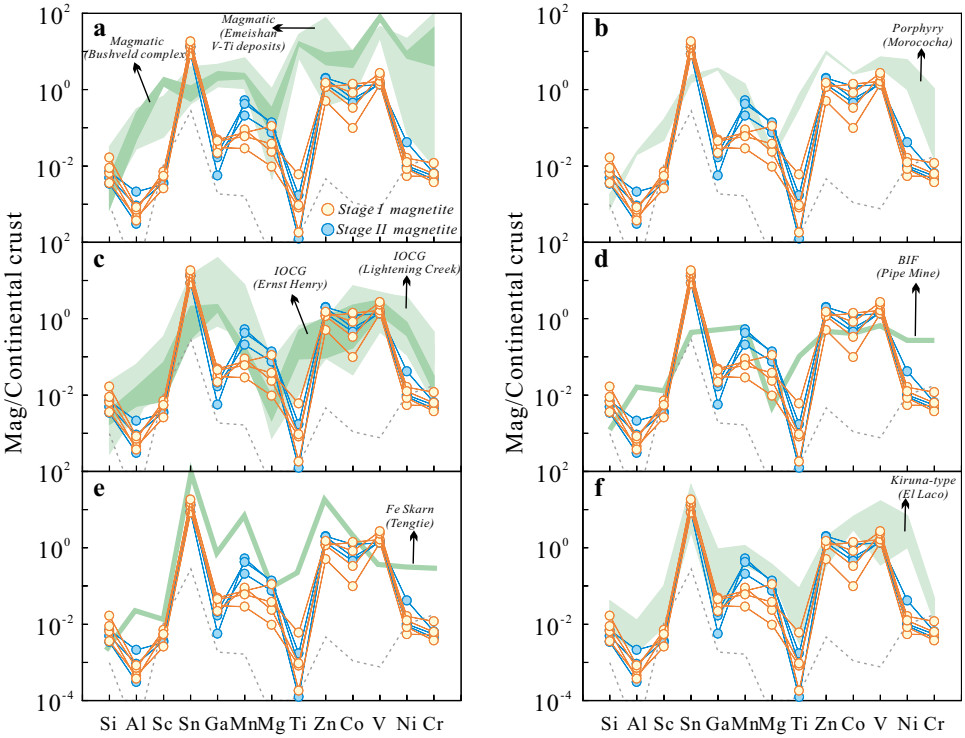

Fig. 6 Continental-crust normalized multiple elements diagrams for the Pingchuan magnetite grains (Stage I and Stage II). Also shown magnetite compositions of magmatic (**a**), porphyry (**b**), IOCG (**c**), BIF (**d**), skarn (**e**) and Kiruna-type (**f**) deposits. The diagrams are designed after Dare et al. (2014). Data are cited from Rudnick and Gao (2003), Carew (2004), Dare et al. (2014), Liu et al. (2015a) and Zhao and Zhou (2015)

Emeishan magmatic magnetite grains. Actually, they are plotted into the field close to hydrothermal magnetite area designed by Nadoll et al. (2015).

Multiple trace elements in magnetite grains were also suggested to be able to identify ore-forming environments and ore deposit types (Dupuis and Beaudoin 2011; Dare et al. 2014; Nadoll et al. 2014; Broughm et al. 2017). In Fig. 6, the Stage I magnetites of the Pingchuan deposit exhibit spiked multiple-element patterns with depletions in Al, Ga, Ti, Ni, and Cr, and enrichments in Sn, Mn, and Zn–Co–V. These patterns are distinct from those of the magmatic magnetite, which have relatively smooth right-inclined patterns with overall high contents of trace elements (Fig. 6a). This comparison precludes purely magmatic-system environments, such as extremely high-temperature, for the Stage I magnetites. Moreover, they are also different from the M-shaped patterns with peaks in Sn–Ga and Ni–V–Co (–Zn) and troughs in Si, Mg and Cr for magnetite from magmatic–hydrothermal porphyry and IOCG (iron-oxide copper and gold) deposits (Fig. 6b, c). The Stage I magnetite grains contain much lower Ni, Ga, Ti, and Al than porphyry and IOCG magnetite. These observations are arguing that magmatic–hydrothermal environments alone could not account for the compositions of the Stage I magnetites. In addition, the Stage I magnetites can be distinguished from BIF magnetite, which shows a relative flat pattern and high Ni–Cr–Ga (Fig. 6d). Interestingly, the Stage I magnetite grains also display enrichments in Sn, Mn, and Zn–Co relative to neighboring elements similar to, although in low level, those of skarn deposits (Fig. 6e). This indicates significant skarn-like wall rock contribution during the generation of the Stage I mineralization. In more details, they show collectively similarities to Kiruna-type magnetite in El Laco except for pronounced lower Ni concentrations (Fig. 6f). Generally, Stage I magnetites have exhibited more affinities with magnetite from Kiruna-type and skarn deposit than other types of deposits.

Previous studies have proposed both magmatic and hydrothermal models for the generation of low-Ti iron deposit within ELIP (Yang 1983; Yao and Yan 1991; Wang et al. 2014; Liu et al. 2015b). Yao and Yan (1991) reported amygdaloidal structures in massive ores of the Niuchang deposit, which located to the south of the Pingchuan deposit. Recently, Liu et al. (2015b) interpreted that these deposits resulted from low-Ti Fe-rich melts separated from low-Ti basaltic magmas based on a Fe_2O_3* drop of 4.51% from gabbro to gabbronorite. However, alteration style, and ore and mineral geochemistry tend to support a hydrothermal origin for the Pingchuan deposit (Yang 1983; Wang et al. 2014). As aforementioned, the Pingchuan deposit exhibits comparable magnetite multiple-element pattern with the Kiruna-type iron deposits in El Laco, which also bear low-Ti features. There are also similar long-living debates over the genesis of Kiruna-type deposits (mainly iron-rich hydrothermal fluids and magmatic iron-rich melts) (see more details in Knipping et al. (2015b). However, a novel model established recently by Knipping et al. (2015a, b) seems to be able to coordinate

the contrasting co-occurrence of purely magmatic and hydrothermal observations. They proposed that magmatic magnetite-bubble suspension separated from magmatic magmas deposit massive magnetite in regional faults. This model actually signifies the role of hydrothermal fluids, consistent with the overall trace-element features of magnetite for Kiruna-type deposits.

In the Pingchuan deposit, Stage I magnetites have hydrothermal origins, arguing against purely magmatic iron-rich melts model. The following lines of evidence also support them to a hydrothermal model for the Pingchuan deposit. (1) Orebodies preferentially occur in the contact zone between limestones and picritic dykes. This is in contrast with the purely magmatic iron-rich melts model, which should expect more spatially association with the regional gabbros (Fig. 2). (2) Ore samples in the Pingchuan deposit contain low P_2O_5 contents (< 1.58%; Table 1) which are crucial for the separation of an iron-rich oxide melts from a Si-rich silicate melt (Hou et al. 2018), arguing against a parental Fe–P-rich melts for the Pingchuan deposit. (3) Gangue minerals are dominated by carbonate minerals (Table 1), identical to the lithology of host rocks. (4) Along with orebodies, extensive alterations (e.g., marmarization) of host rocks have been observed (Fig. 3a). More skarn minerals, such as diopside, actinolite, and epidote, have been documented in the ore district (Wang et al. 2014). (5) Abundant gangue mineral inclusions, e.g., carbonate minerals, occur in Stage I magnetites (Fig. 4), which is common in the hydrothermal system. (6) Some Stage I magnetite grains in the Pingchuan deposit exhibit oscillatory zones, similar to the typical structure for skarn-type high-temperature magnetite (Zhao and Zhou 2015). (7) The $\delta^{18}O$ values of magnetite (although we do not know which stage they belong to) in this deposit are consistent with magmatic-water origin rather than pure mantle-derived magma origin (Wang et al. 2014). Therefore, hydrothermal fluids are crucial for the generation of the Pingchuan deposit.

The enrichment in Sn–Mn–Zn are typical features of skarn magnetite (Fig. 6e). Along with the emplacement of picritic dykes, primary ore-forming fluids reacted with limestones, depositing the Sn–Mn–Zn-rich Stage I magnetite grains with accessory apatite. During the Cenozoic fault activities, previously formed minerals suffered from fragmentation and inclusion-rich Stage II magnetite grains were generated. These fluids contain abundant carbonate components and lead to more elevated Mn–Al in Stage II magnetite grains relative to previous magnetite grains. This possibly indicates that the fluids have more contributions from carbonate wall rocks, might consistent with the presence of hydrothermal carbonate veins in breccia rocks in the ore district. Although the magmatic magnetite-bubble suspension model (Knipping et al. 2015a, b) could not be precluded, we still infer that the Pingchuan deposit is hydrothermal in origin on the bias of available data. The early ore-forming fluids were possibly magmatic–hydrothermal in origin, whereas the late fluids might be induced from fault activity. However, it still requires more studies on the nature of ore-forming fluids to explain chemical divergences, such Al–Ti–Ni–Cr, between the Pingchuan and typical skarn magnetite.

6 Conclusion

Two stages of magnetite grains were identified in the Pingchuan iron deposit: early fragmented, euhedral–subhedral, large-sized magnetite grains and late unfragmented anhedral, small-sized magnetite grains. They correspond to Permian magmatism and Cenozoic thermal event. Both the early and late magnetite grains show signatures of hydrothermal magnetite, which supports a hydrothermal origin for the deposit. Contributions from carbonate wall rocks are significant in the ore-forming processes.

Acknowledgements This study was supported by the National Natural Science Foundation of China (Grants 41572074 and 41273049) and the Strategic Priority Research Program of the Chinese Academy of Sciences (Grant No. XDB18030204). We thank Dr. Zhihui Dai for her assistance in magnetite analyses using LA-ICP-MS. Local engineers from the Pingchuan deposit are also appreciated for their help in field work.

Appendix

LA-ICP-MS trace elemental compositions of magnetite from the Pingchuan deposit in the ELIP

Sample		DB1420						
Analysis		DB1420-1	DB1420-2	DB1420-3	DB1420-4	DB1420-5	DB1420-6	DB1420-7
Description		Stage I	Stage I	Stage I	Stage I	Stage I	Stage I	Stage I
Na	ppm	22.9	3.75	13.2	8.06	1.53	1.66	2.71
Mg	ppm	2330	416	3189	812	2783	7158	5283
Al	ppm	22.6	43.9	73.9	46.3	37.6	26.1	14.3
Si	ppm	848	846	900	1377	1525	756	765
P	ppm	74.9	11.8	13.1	–	11.0	2.72	19.4
Ca	ppm	150	46.3	33.0	143	60.6	50.1	69.9
Ti	ppm	2.44	0.72	0.47	0.68	0.97	0.00	0.00
Mn	ppm	263	31.7	41.1	26.3	14.6	21.0	9.4
Sc	ppm	–	0.07	–	0.07	–	0.03	–
V	ppm	122	135	180	157	276	254	195
Cr	ppm	–	0.12	1.31	–	–	–	–
Co	ppm	1.69	0.30	6.73	0.33	3.01	4.36	1.81
Ni	ppm	0.15	0.92	0.62	0.44	0.08	0.01	0.04
Cu	ppm	0.10	0.01	–	0.06	0.02	–	0.18
Zn	ppm	21.5	15.8	80.0	13.8	26.4	57.5	35.9
Ga	ppm	0.92	1.01	0.42	0.85	0.90	0.55	0.82
Ge	ppm	0.09	0.24	0.34	0.09	2.44	0.10	0.11
Rb	ppm	–	0.01	0.03	0.01	0.02	0.01	0.01
Sr	ppm	2.35	0.13	1.56	0.30	0.63	0.01	0.38
Y	ppm	0.50	0.12	0.08	0.35	0.12	0.22	0.26
Zr	ppm	0.11	–	0.04	–	0.05	18.4	0.05
Nb	ppm	1.67	2.12	3.31	4.42	3.19	2.00	1.64
Mo	ppm	0.03	0.05	–	–	–	–	0.01
Ag	ppm	–	0.03	–	0.01	–	0.01	–
Cd	ppm	0.03	–	0.09	–	1.82	0.05	0.04
In	ppm	0.09	0.13	0.20	0.20	0.11	0.33	0.11
Sn	ppm	11.1	17.9	10.7	17.1	15.4	13.4	13.4
Ba	ppm	17.4	0.37	8.42	1.26	2.93	0.07	2.69
Hf	ppm	–	0.01	–	–	–	0.01	–
Ta	ppm	–	0.01	–	–	–	–	–
W	ppm	0.01	0.03	–	0.17	0.14	–	0.02
Bi	ppm	0.02	–	0.01	–	–	0.01	–
Pb	ppm	0.22	–	0.09	–	–	–	0.03
Th	ppm	–	–	0.01	–	–	–	0.01
U	ppm	0.08	0.03	–	0.09	0.03	0.04	0.01
Al + Mn	wt%	0.029	0.008	0.012	0.007	0.005	0.005	0.002
Ti + V	wt%	0.012	0.014	0.018	0.016	0.028	0.025	0.019

Sample		DB1430							
Analysis		DB1430-1	DB1430-2	DB1430-3	DB1430-4	DB1430-5	DB1430-6	DB1430-7	DB1430-8
Description		Stage I	Stage I	Stage I	Stage I	Stage I	Stage I	Stage I	Stage I
Na	ppm	0.00	4.89	5.43	0.07	0.00	12.1	0.00	3.22
Mg	ppm	39.4	975	623	9.16	4.66	459	7.42	35.7
Al	ppm	39.5	89.3	41.2	24.8	13.9	17.1	12.0	12.6
Si	ppm	709	3923	2969	1069	1277	2495	678	1653
P	ppm	23.0	9.08	11.0	52.1	25.7	25.6	3.07	24.8
Ca	ppm	33.6	1527	573	62.6	4.55	652	33.2	57.7
Ti	ppm	2.44	0.12	11.9	0.54	3.22	3.62	1.08	4.37
Mn	ppm	14.5	47.4	38.4	13.2	9.19	27.4	14.0	12.4
Sc	ppm	0.12	–	–	0.21	0.07	0.12	–	0.07
V	ppm	118	326	309	184	288	195	119	276
Cr	ppm	0.43	–	0.15	0.46	5.83	1.75	–	0.95

continued

Sample		DB1430							
Analysis		DB1430-1	DB1430-2	DB1430-3	DB1430-4	DB1430-5	DB1430-6	DB1430-7	DB1430-8
Description		Stage I	Stage I	Stage I	Stage I	Stage I	Stage I	Stage I	Stage I
Co	ppm	36.3	37.5	38.1	37.4	37.6	38.5	37.3	36.5
Ni	ppm	–	0.85	2.85	0.18	1.88	0.39	0.25	0.22
Cu	ppm	–	–	–	0.03	–	–	–	0.19
Zn	ppm	85.4	107	94.7	72.9	64.7	76.7	82.2	82.6
Ga	ppm	0.39	0.70	0.33	0.59	0.33	0.60	0.51	0.44
Ge	ppm	0.36	0.28	–	–	–	0.29	0.20	–
Rb	ppm	–	0.02	0.01	–	–	–	0.01	–
Sr	ppm	–	0.38	0.09	–	–	0.12	0.01	–
Y	ppm	0.20	13.46	4.04	0.21	0.20	5.03	0.35	0.21
Zr	ppm	0.16	0.02	–	0.10	–	–	–	–
Nb	ppm	1.55	46.7	12.6	1.66	5.19	20.7	1.51	3.58
Mo	ppm	–	0.02	–	–	–	–	–	0.08
Ag	ppm	–	–	0.01	0.02	0.01	0.03	0.02	0.02
Cd	ppm	–	0.05	0.08	0.03	–	0.07	0.02	–
In	ppm	0.07	0.16	0.14	0.04	0.05	0.19	0.10	0.09
Sn	ppm	14.8	29.7	27.4	12.8	14.5	29.5	17.0	21.8
Ba	ppm	–	0.08	–	–	–	0.05	0.02	0.21
Hf	ppm	–	–	–	–	0.03	–	–	–
Ta	ppm	–	–	–	–	–	–	–	–
W	ppm	0.02	–	–	–	–	0.02	–	0.01
Bi	ppm	–	0.01	0.01	0.01	–	0.01	–	0.02
Pb	ppm	–	0.02	–	–	–	0.04	–	4.21
Th	ppm	0.01	3.40	0.01	0.06	–	–	0.02	–
U	ppm	0.08	1.54	0.51	0.04	0.02	0.50	0.02	0.15
Al + Mn	wt%	0.005	0.014	0.008	0.004	0.002	0.004	0.003	0.002
Ti + V	wt%	0.012	0.033	0.032	0.018	0.029	0.020	0.012	0.028

Sample		DB1431							
Analysis		DB1431-1	DB1431-2	DB1431-3	DB1431-4	DB1431-5	DB1431-6	DB1431-7	DB1431-8
Description		Stage I	Stage I	Stage I	Stage I	Stage I	Stage I	Stage I	Stage I
Na	ppm	61.4	2.43	7.22	12.4	7.79	2.01	3.27	4.37
Mg	ppm	1184	62.4	705	744	694	584	491	809
Al	ppm	19.7	37.6	92.1	97.4	85.9	68.6	37.3	42.2
Si	ppm	868	1608	3012	3128	3136	2572	2438	3286
P	ppm	18.8	32.4	42.5	–	18.1	34.4	–	13.2
Ca	ppm	130	–	720	750	870	487	406	722
Ti	ppm	6.21	–	0.16	0.69	0.00	10.35	5.99	–
Mn	ppm	322	11.7	37.4	41.7	35.3	35.1	26.3	41.1
Sc	ppm	0.13	–	0.11	0.09	0.22	0.17	–	0.20
V	ppm	199	335	370	370	375	346	292	288
Cr	ppm	–	0.02	0.86	0.58	0.18	1.01	–	0.38
Co	ppm	13.3	7.61	8.32	9.68	8.60	8.01	7.33	7.08
Ni	ppm	0.66	0.14	0.89	0.54	0.92	0.36	0.42	0.03
Cu	ppm	1.01	–	0.07	0.06	–	0.14	0.05	–
Zn	ppm	73.7	79.1	81.0	85.1	87.0	85.1	75.3	97.4
Ga	ppm	0.29	0.21	0.36	0.42	0.39	0.36	0.36	0.39
Ge	ppm	–	0.02	0.01	0.37	0.37	–	–	0.18
Rb	ppm	0.02	0.01	–	0.02	0.07	0.01	–	–
Sr	ppm	0.41	0.01	0.17	0.21	0.22	0.12	0.11	0.17
Y	ppm	0.63	0.22	7.00	7.95	8.04	3.08	2.37	4.09
Zr	ppm	–	0.02	0.04	0.05	0.14	–	–	–
Nb	ppm	2.76	3.07	31.8	33.9	50.8	78.8	36.7	165

continued

Sample		DB1431							
Analysis		DB1431-1	DB1431-2	DB1431-3	DB1431-4	DB1431-5	DB1431-6	DB1431-7	DB1431-8
Description		Stage I	Stage I	Stage I	Stage I	Stage I	Stage I	Stage I	Stage I
Mo	ppm	–	0.03	–	–	13.5	0.02	–	0.02
Ag	ppm	0.03	0.01	–	–	–	–	–	0.03
Cd	ppm	–	0.04	0.06	–	–	–	0.08	–
In	ppm	0.10	0.10	0.12	0.13	0.13	0.15	0.11	0.21
Sn	ppm	21.1	17.0	25.7	25.6	25.3	26.4	28.8	34.5
Ba	ppm	1.45	–	–	0.12	0.09	–	1.78	0.08
Hf	ppm	0.01	–	–	0.01	–	–	0.01	0.03
Ta	ppm	–	–	–	–	–	–	–	–
W	ppm	–	0.01	–	0.02	0.03	–	0.01	0.02
Bi	ppm	–	0.01	0.01	–	0.01	0.01	0.01	0.02
Pb	ppm	–	–	–	–	0.07	–	–	0.02
Th	ppm	0.01	0.01	0.03	–	0.05	0.03	0.01	0.01
U	ppm	0.03	0.03	0.50	0.51	0.77	0.25	0.23	0.35
Al + Mn	wt%	0.034	0.005	0.013	0.014	0.012	0.010	0.006	0.008
Ti + V	wt%	0.021	–	0.037	0.037	0.038	0.036	0.030	–

Sample		DB1432								DB1402		
Analysis		DB1432-1	DB1432-2	DB1432-3	DB1432-4	DB1432-5	DB1432-6	DB1432-7	DB1432-8	DB1402-1	DB1402-2	DB1402-3
Description		Stage I	Stage I	Stage I	Stage I	Stage I	Stage I	Stage I	Stage I	Stage II	Stage II	Stage II
Na	ppm	36.7	18.1	16.9	16.1	4.97	4.26	10.4	10.7	5.92	–	0.22
Mg	ppm	1428	1751	1210	1137	756	819	493	1002	2421	6251	1841
Al	ppm	88.4	118	98.5	129	31.3	20.7	27.8	44.5	19.6	22.7	34.5
Si	ppm	6317	7561	5426	5310	3009	2999	2759	4277	981	1146	768
P	ppm	75.4	61.5	74.4	39.2	–	–	6.87	11.0	21.6	49.4	46.5
Ca	ppm	2376	3136	2141	1692	201	67.9	599	1620	81.3	2.50	46.2
Ti	ppm	–	17.6	30.3	67.5	32.0	7.40	15.1	4.47	19.9	0.61	0.96
Mn	ppm	60.5	67.6	57.9	59.3	33.8	29.2	25.3	37.1	149	871	192
Sc	ppm	0.01	0.03	0.31	0.28	0.06	0.14	–	0.02	–	–	–
V	ppm	475	522	365	371	355	118	389	373	184	235	141
Cr	ppm	1.71	–	0.71	0.16	–	1.02	0.80	0.66	–	1.11	0.62
Co	ppm	23.0	22.4	22.7	21.8	21.5	21.7	20.6	20.8	25.9	47.7	24.0
Ni	ppm	0.86	0.26	1.20	0.52	0.85	0.38	0.81	1.02	6.21	0.44	0.70
Cu	ppm	0.06	0.02	0.14	0.35	0.01	0.02	0.10	–	0.08	0.01	–
Zn	ppm	112	121	134	116	97.3	107	79.5	95.4	137	184	110
Ga	ppm	0.89	1.05	0.98	0.72	0.26	0.46	0.38	1.01	0.12	0.11	0.04
Ge	ppm	–	0.53	0.10	0.48	0.04	0.23	0.07	–	–	–	–
Rb	ppm	0.01	0.90	0.02	–	0.01	0.01	–	–	–	–	0.01
Sr	ppm	1.30	1.43	0.79	0.47	0.05	–	0.09	0.39	0.11	0.01	
Y	ppm	21.6	29.4	19.1	12.2	1.42	0.58	4.33	13.6	0.15	0.05	0.10
Zr	ppm	0.08	0.21	0.29	0.17	–	–	0.03	5.65	1.40	0.06	–
Nb	ppm	162	215	128	213	10.4	6.41	16.8	56.3	3.07	3.44	1.31
Mo	ppm	–	–	–	0.10	1.04	–	–	0.02	0.13	0.15	0.20
Ag	ppm	0.01	0.01	0.01	0.01	0.05	0.01	0.01	–	0.01	0.01	0.01
Cd	ppm	–	–	0.13	0.05	–	0.15	0.05	–	0.14	0.07	–
In	ppm	0.20	0.22	0.17	0.17	0.15	0.17	0.10	0.13	0.19	0.22	0.07
Sn	ppm	34.9	38.2	25.4	28.3	29.8	36.0	25.2	28.7	20.9	14.5	8.32
Ba	ppm	0.32	0.26	0.08	0.06	–	–	0.08	0.10	0.15	0.09	–
Hf	ppm	–	–	0.02	0.07	–	–	–	–	0.05	–	0.01
Ta	ppm	0.03	0.04	0.01	0.01	–	–	–	–	0.01	0.02	–
W	ppm	0.02	–	–	–	–	0.03	–	–	0.15	0.01	–
Bi	ppm	–	–	–	0.01	0.01	0.01	0.01	–	0.07	0.01	–
Pb	ppm	–	–	–	0.05	0.02	–	0.05	–	0.05	0.05	–

continued

Sample		DB1432								DB1402		
Analysis		DB1432-1	DB1432-2	DB1432-3	DB1432-4	DB1432-5	DB1432-6	DB1432-7	DB1432-8	DB1402-1	DB1402-2	DB1402-3
Description		Stage I	Stage I	Stage I	Stage I	Stage I	Stage I	Stage I	Stage I	Stage II	Stage II	Stage II
Th	ppm	0.04	0.12	0.25	0.14	–	–	0.02	0.06	–	–	–
U	ppm	3.83	5.75	1.64	1.16	0.12	0.04	0.32	1.06	0.43	0.03	0.01
Al + Mn	wt%	0.015	0.019	0.016	0.019	0.007	0.005	0.005	0.008	0.017	0.089	0.023
Ti + V	wt%	–	0.054	0.040	0.044	0.039	0.013	0.040	0.038	0.020	0.024	0.014

Sample		DB1426							
Analysis		DB1426-1	DB1426-2	DB1426-3	DB1426-4	DB1426-5	DB1426-6	DB1426-7	DB1426-8
Description		Stage II	Stage II	Stage II	Stage II	Stage II	Stage II	Stage II	Stage II
Na	Ppm	5.10	1.48	27.9	2.66	1.21	0.00	2.97	9.47
Mg	ppm	5722	1392	2496	209	2161	68.9	3652	1223
Al	ppm	100	49.1	22.0	53.9	80.0	28.7	19.3	257
Si	ppm	1598	1022	624	1063	1241	676	1511	3341
P	ppm	0.00	13.2	28.6	5.27	33.9	13.7	29.4	39.7
Ca	ppm	261	0.00	103	74.7	51.0	78.8	198	437
Ti	ppm	0.20	0.16	1.95	–	0.18	0.14	–	0.42
Mn	ppm	759	39.8	219	16.3	55.6	16.6	105	72.7
Sc	ppm	–	–	–	–	–	0.08	0.09	0.06
V	ppm	93.6	238	112	174	305	115	157	363
Cr	ppm	–	0.91	–	0.35	0.05	1.66	–	–
Co	ppm	28.1	12.5	17.8	12.0	14.0	12.4	13.7	11.5
Ni	ppm	0.02	1.16	0.44	0.37	0.72	0.13	0.45	0.98
Cu	ppm	–	–	–	–	0.08	0.04	–	0.13
Zn	ppm	440	51.6	143	229	52.9	27.5	155	17.2
Ga	ppm	0.15	0.24	0.25	0.28	0.19	0.35	0.11	0.59
Ge	ppm	0.06	0.24	–	–	0.23	0.08	0.26	0.21
Rb	ppm	0.38	0.01	0.01	–	–	0.01	0.01	–
Sr	ppm	0.03	0.01	1.93	0.09	–	0.01	0.34	0.11
Y	ppm	0.26	0.16	0.20	0.13	0.15	0.14	1.16	3.21
Zr	ppm	0.04	0.04	0.03	–	–	–	0.06	–
Nb	ppm	42.7	3.39	3.62	2.15	5.19	2.03	4.33	8.77
Mo	ppm	0.03	–	0.01	0.02	0.05	0.05	–	–
Ag	ppm	0.01	0.01	–	0.01	–	0.02	0.03	–
Cd	ppm	0.15	0.07	0.02	–	0.08	0.13	0.07	0.22
In	ppm	0.59	0.05	0.11	0.17	0.10	0.06	0.27	0.23
Sn	ppm	69.7	12.2	12.6	10.5	18.0	10.7	20.5	20.3
Ba	ppm	0.05	0.77	18.7	0.35	–	–	–	0.39
Hf	ppm	–	–	0.01	–	–	0.01	–	–
Ta	ppm	0.02	–	–	–	0.03	–	–	–
W	ppm	0.01	0.01	0.02	0.04	–	–	0.01	0.01
Bi	ppm	–	–	0.01	0.02	–	0.01	0.03	–
Pb	ppm	0.02	0.04	0.07	0.55	–	0.01	0.01	–
Th	ppm	–	0.05	–	–	–	–	–	–
U	ppm	0.25	0.04	0.25	0.03	0.05	0.04	0.14	0.28
Al + Mn	wt%	0.086	0.009	0.024	0.007	0.014	0.005	0.012	0.033
Ti + V	wt%	0.009	0.024	0.011	–	0.031	0.012	–	0.036

continued

Sample		DB1427					D.L.
Analysis		DB1427-1	DB1427-2	DB1427-3	DB1427-4	DB1427-5	
Description		Stage II	Stage II	Stage II	Stage II	Stage II	
Na	Ppm	82.7	261	28.5	83.7	27.7	2.30
Mg	ppm	5165	896	6998	5208	998	1.19
Al	ppm	212	252	179	83.2	165	1.18
Si	ppm	2557	1155	3378	1899	864	269
P	ppm	38.7	23.5	35.6	51.3	32.9	51.2
Ca	ppm	506	581	1874	555	31.1	89.2
Ti	ppm	3.58	6.52	1.10	1.28	5.28	0.747
Mn	ppm	269	151	530	521	146	1.205
Sc	ppm	–	0.02	0.12	0.07	0.08	0.270
V	ppm	160	232	191	265	168	0.141
Cr	ppm	1.21	0.96	0.91	0.44	0.14	2.468
Co	ppm	7.51	1.83	15.6	30.3	4.16	0.031
Ni	ppm	–	1.61	0.53	0.02	0.21	0.537
Cu	ppm	0.46	–	0.07	0.09	–	0.347
Zn	ppm	85.9	108	90.2	163	39.3	0.348
Ga	ppm	0.28	0.44	0.47	0.17	0.32	0.036
Ge	ppm	0.22	0.50	0.26	0.06	–	0.440
Rb	ppm	0.05	0.06	–	0.07	0.02	0.033
Sr	ppm	1.27	6.94	2.39	3.75	1.38	0.003
Y	ppm	1.73	0.45	6.76	1.66	0.14	0.003
Zr	ppm	0.14	0.08	0.39	–	0.20	0.061
Nb	ppm	6.55	8.94	28.8	18.5	4.46	0.002
Mo	ppm	0.03	0.36	–	0.07	0.09	0.008
Ag	ppm	0.02		–	–	–	0.025
Cd	ppm	–	0.18	–	0.11	0.04	0.066
In	ppm	0.34	0.21	0.35	0.28	0.11	0.016
Sn	ppm	27.8	18.5	26.9	21.7	19.1	0.588
Ba	ppm	5.45	15.23	0.75	7.24	2.82	0.032
Hf	ppm	0.01	–	–	–	–	0.012
Ta	ppm	0.08	0.01	0.01	–	0.01	0.003
W	ppm	0.02	0.06	–	0.07	0.01	0.015
Bi	ppm	0.01	0.04	–	0.01	–	0.008
Pb	ppm	0.15	1.58	–	0.22	–	0.053
Th	ppm	0.04	–	–	–	–	0.009
U	ppm	0.59	0.58	1.65	0.36	0.47	0.007
Al + Mn	wt%	0.048	0.040	0.071	0.060	0.031	
Ti + V	wt%	0.016	0.024	0.019	0.027	0.017	

References

Ali JR, Thompson GM, Zhou MF, Song XY (2005) Emeishan large igneous province, SW China. Lithos 79:475–489

Bai ZJ, Zhong H, Li C, Zhu WG, Xu GW (2012a) Platinum-group elements in the oxide layers of the Hongge mafic–ultramafic intrusion, Emeishan Large Igneous Province, SW China. Ore Geol Rev 46:149–161

Bai ZJ, Zhong H, Naldrett AJ, Zhu WG, Xu GW (2012b) Whole-rock and mineral composition constraints on the genesis of the giant Hongge Fe–Ti–V oxide deposit in the Emeishan Large Igneous Province, Southwest China. Econ Geol 107:507–524

Broughm SG, Hanchar JM, Tornos F, Westhues A, Attersley S (2017) Mineral chemistry of magnetite from magnetite-apatite mineralization and their host rocks: examples from Kiruna, Sweden, and El Laco, Chile. Miner Depos 52:1223–1244

Carew MJ (2004) Controls on Cu–Au mineralization and Fe oxide metasomatism in the Eastern Fold Belt, N.W. Queensland, Australia. Ph.D thesis, James Cook University, Queensland

Chen LM, Song XY, Zhu XK, Zhang XQ, Yu SY, Yi JN (2014) Iron isotope fractionation during crystallization and sub-solidus re-equilibration: constraints from the Baima mafic layered intrusion, SW China. Chem Geol 380:97–109

Chung SL, Jahn BM (1995) Plume–lithosphere interaction in generation of the Emeishan flood basalts at the Permian–Triassic boundary. Geology 23:889–892

Dare SAS, Barnes SJ, Beaudoin G, Meric J, Boutroy E, Potvin-Doucet C (2014) Trace elements in magnetite as petrogenetic indicators. Miner Depos 49:785–796

Dupuis C, Beaudoin G (2011) Discriminant diagrams for iron oxide trace element fingerprinting of mineral deposit types. Miner Depos 46:319–335

Einaudi MT, Hedenquist JW, Inan EE (2003) Sulfidation state of fluids in active and extinct hydrothermal systems: transitions from porphyry to epithermal environments. Soc Econ Geol Spec Publ 10:285–313

Gao JF, Zhou MF, Lightfoot PC, Wang CY, Qi L, Sun M (2013) Sulfide saturation and magma emplacement in the formation of the Permian Huangshandong Ni–Cu sulfide deposit, Xinjiang, northwestern China. Econ Geol 108:1833–1848

Ge XH (1984) A discussion on nappe structure in Yanyuan, west Sichuan. J Jilin Univ (Earth Sci Ed) 1:36–43 **(in Chinese with English abstract)**

Hou T, Charlier B, Holtz F, Veskler I, Zhang ZC, Thomas R, Namur O (2018) Immiscible hydrous Fe–Ca–P melt and the origin of iron oxide-apatite ore deposits. Nat Commun 9:1415

Knipping JL, Bilenker LD, Simon AC, Reich M, Barra F, Deditius AP, Lundstrom C, Bindeman I, Munizaga R (2015a) Giant Kiruna-type deposits form by efficient flotation of magmatic magnetite suspensions. Geology 43:591–594

Knipping JL, Bilenker LD, Simon AC, Reich M, Barra F, Deditius AP, Wälle M, Heinrich CA, Holtz F, Munizaga R (2015b) Trace elements in magnetite from massive iron oxide-apatite deposits indicate a combined formation by igneous and magmatic–hydrothermal processes. Geochim Cosmochim Acta 171:15–38

Li ZX, Li XH, Kinny PD, Wang J, Zhang S, Zhou H (2003) Geochronology of Neoproterozoic syn-rift magmatism in the Yangtze Craton, South China and correlations with other continents: evidence for a mantle superplume that broke up Rodinia. Precambrian Res 122:85–109

Li XH, Li ZX, Sinclair JA, Li WX, Carter G (2006) Revisiting the "Yanbian Terrane": implications for Neoproterozoic tectonic evolution of the western Yangtze Block, South China. Precambrian Res 151:14–30

Liu YS, Hu ZC, Gao S, Gunther D, Xu J, Gao CG, Chen HH (2008) In situ analysis of major and trace elements of anhydrous minerals by LA-ICP-MS without applying an internal standard. Chem Geol 257:34–43

Liu PP, Zhou MF, Chen WT, Gao JF, Huang XW (2015a) In-situ LA-ICP-MS trace elemental analyses of magnetite: Fe–Ti–(V) oxide-bearing mafic–ultramafic layered intrusions of the Emeishan Large Igneous Province, SW China. Ore Geol Rev 65:853–871

Liu WH, Zhang J, Sun T, Zhou L, Liu AL (2015b) Low-Ti iron oxide deposits in the Emeishan large igneous province related to low-Ti basalts and gabbroic intrusions. Ore Geol Rev 65:180–197

Ma Y, Ji XT, Li JC, Huang M, Kan ZZ (2003) Mineral resources of the Panzhihua region. Sichuan Science and Technology Press, Chengdu, p 275 **(in Chinese)**

Nadoll P, Angerer T, Mauk JL, French D, Walshe J (2014) The chemistry of hydrothermal magnetite: a review. Ore Geol Rev 61:1–32

Nadoll P, Mauk JL, Leveille RA, Koenig AE (2015) Geochemistry of magnetite from porphyry Cu and skarn deposits in the southwestern United States. Miner Depos 50:493–515

Panxi Geological Team (1982) Detailed geological prospecting report of Kungshangliangzi iron ore in Yanyuan country, Sichuan province. Unpublished p 25 **(in Chinese)**

Rudnick R, Gao S (2003) Composition of the continental crust. Treatise Geochem 3:1–64

SBGMR (Sichuan Bureau of Geology and Mineral Resources) (1991) Regional geology of Sichuan province. Geological Publishing House, Beijing, p 680 **(in Chinese)**

Shellnutt JG, Denyszyn SW, Mundil R (2012) Precise age determination of mafic and felsic intrusive rocks from the Permian Emeishan Large Igneous Province (SW China). Gondwana Res 22:118–126

Song XY, Zhang CJ, Hu RZ, Zhong H, Zhou MF, Ma RZ, Li YG (2005) Genetic links of magmatic deposits in the Emeishan large igneous province with dynamics of mantle plume. J Mineral Petrol 25(4):35–44 **(in Chinese with English abstract)**

Song XY, Keays RR, Xiao L, Qi HW, Ihlenfeld C (2009) Platinum-group element geochemistry of the continental flood basalts in the central Emeisihan Large Igneous Province, SW China. Chem Geol 262:246–261

Song XY, Qi HW, Hu RZ, Chen LM, Yu SY, Zhang JF (2013) Formation of thick stratiform Fe–Ti oxide layers in layered intrusion and frequent replenishment of fractionated mafic magma: evidence from the Panzhihua intrusion, SW China. Geochem Geophys Geosyst 14:712–732

Wang M, Zhang ZC, Encarnacion J, Hou T, Luo WJ (2012) Geochronology and geochemistry of the Nantianwan mafic–ultramafic complex, Emeishan large igneous province: metallogenesis of magmatic Ni–Cu sulphide deposits and geodynamic setting. Int Geol Rev 54:1746–1764

Wang M, Zhang ZC, Santosh M, Hou T (2014) Geochemistry of Late Permian picritic porphyries and associated Pingchuan iron ores, Emeishan Large Igneous Province, Southwest China: constraints on petrogenesis and iron sources. Ore Geol Rev 57:602–617

Wang YC, Gao JF, Huang XW, Qi L, Lyu C (2018) Trace element composition of magnetite from the Xinqiao Fe–S(–Cu–Au) deposit, Tongling, Eastern China: constraints on fluid evolution and ore genesis. Acta Geochim 37(5):639–654

Yang SH (1983) Approach to character and genesis of magnetite from Kuangshanliangzi magnetite deposit, Yanyuan, Sichuan. Bull Chengdu Inst Geol M R Chin Acad Geol Sci 4:33–43 **(in Chinese with English abstract)**

Yao ZD, Yan YQ (1991) A further understanding on genesis of the Kuangshanliangzi–Niuchang magnetite deposits in Yanyuan region, Sichuan Province. Acta Geol Sichuan 11(2):117–126 **(in Chinese)**

Zeng LG, Zhang J, Sun T, Guo DB (2013) Zircon U–Pb age of mafic–ultramafic rock from Pingchuan region in Southern Sichuan and its geological implications. Earth Sci J China Univ Geosci 38(6):1197–1213 **(in Chinese with English abstract)**

Zhang ZC, Mahoney JJ, Mao JW, Wang FS (2006) Geochemistry of picritic and associated basalt flows of the western Emeishan flood basalt province, China. J Petrol 47:1997–2019

Zhao WW, Zhou MF (2015) In-situ LA-ICP-MS trace elemental analyses of magnetite: the Mesozoic Tengtie skarn Fe deposit in the Nanling Range, South China. Ore Geol Rev 65:872–883

Zhong KH, Liu ZC, Shi YS, Li FY, Shu LS (2004) Yanyuan-Lijiang tectonic zone: a Cenozoic intracontinental orogenic belt. Acta Geol Sin 78(1):36–43 **(in Chinese with English abstract)**

Zhong H, Qi L, Hu RZ, Zhou MF, Gou TZ, Zhu WG, Liu BG, Chu ZY (2011) Rhenium–osmium isotope and platinum-group elements in the Xinjie layered intrusion, SW China: Implications for source mantle composition, mantle evolution, PGE fractionation and mineralization. Geochim Cosmochim Acta 75:1621–1641

Zhou MF, Robinson PT, Lesher CM, Keays RR, Zhang CJ, Malpas J (2005) Geochemistry, petrogenesis and metallogenesis of the Panzhihua gabbroic layered intrusion and associated Fe–Ti–V oxide deposits, Sichuan Province, SW China. J Petrol 46:2253–2280

Zhou MF, Ma YX, Yan DP, Xia XP, Zhao JH, Sun M (2006) The Yanbian terrane (southern Sichuan Province, SW China): a Neoproterozoic arc assemblage in the western margin of the Yangtze Block. Precambrian Res 144:19–38